SUPERCONDUCTIVITY

Electrically tunable low-density superconductivity in a monolayer topological insulator

Valla Fatemi[1]*, Sanfeng Wu[1]*†, Yuan Cao[1], Landry Bretheau[2], Quinn D. Gibson[3], Kenji Watanabe[4], Takashi Taniguchi[4], Robert J. Cava[5], Pablo Jarillo-Herrero[1]†

Turning on superconductivity in a topologically nontrivial insulator may provide a route to search for non-Abelian topological states. However, existing demonstrations of superconductor-insulator switches have involved only topologically trivial systems. Here we report reversible, in situ electrostatic on-off switching of superconductivity in the recently established quantum spin Hall insulator monolayer tungsten ditelluride (WTe_2). Fabricated into a van der Waals field-effect transistor, the monolayer's ground state can be continuously gate-tuned from the topological insulating to the superconducting state, with critical temperatures T_c up to ~1 kelvin. Our results establish monolayer WTe_2 as a material platform for engineering nanodevices that combine superconducting and topological phases of matter.

The intersection of superconductivity and topological insulators hosts a fertile landscape of interesting quantum phenomena, including non-Abelian topological excitations (*1*–*3*). Some topological insulators have been turned into superconductors via chemical doping (*4*, *5*), application of pressure (*6*–*8*), or via the proximity effect (*9*, *10*), methods that are either irreversible or ex situ. Proximity effect–based devices have, in particular, been engineered in an effort to realize Majorana physics; this has required fine-tuned interface engineering between distinct materials (*11*–*16*).

Here we report the observation of intrinsic superconductivity in the monolayer topological insulator WTe_2 induced by the electric field effect. This monolayer transition metal dichalcogenide has recently been established as a quantum spin Hall insulator with robust edge transport up to 100 K (*17*–*22*). Our field-effect device geometry (*23*) is illustrated in Fig. 1, A and B. The WTe_2 monolayer flake is van der Waals–encapsulated between two sheets of hexagonal boron nitride (BN) to protect it from chemical degradation and to improve transport characteristics. Top and bottom electrostatic gates, for which the same BN sheets serve as gate dielectrics, are fabricated to modulate the carrier density. An optical microscopy image of a typical device (device 1, with BN thicknesses of 15 nm, top, and 8 nm, bottom) is shown in Fig. 1B.

[1]Department of Physics, Massachusetts Institute of Technology, Cambridge, MA 02139, USA. [2]Laboratoire des Solides Irradiés, École Polytechnique, CNRS, CEA, 91128 Palaiseau Cedex, France. [3]Department of Chemistry, University of Liverpool, Liverpool L69 7ZX, UK. [4]Advanced Materials Laboratory, National Institute for Materials Science, 1-1 Namiki, Tsukuba 305-0044, Japan. [5]Department of Chemistry, Princeton University, Princeton, NJ 08544, USA.
*These authors contributed equally to this work.
†Corresponding author. Email: swu02@mit.edu (S.W.); pjarillo@mit.edu (P.J.-H.)

Figure 1C displays the temperature dependence of the four-probe resistance $R(T)$ in device 1 when the monolayer is n-doped [bottom-gate voltage (V_{bg}) = 4 V; top-gate voltage (V_{tg}) = 5 V]. R drops to zero at low temperatures from 1.2 kilohm in the normal state, and this zero-resistance state is present for a wide range of gate-voltage parameters (inset of Fig. 1C). The dc voltage-current (V-I) characteristics at various temperatures (Fig. 1D) exhibit the transition from ohmic behavior (red curve) at ~1 K to highly nonlinear behavior (black curve) at low temperatures, including the characteristic zero-voltage plateau for finite current, typical of superconductivity. This nonlinearity is further captured by the measurement shown in Fig. 1E, where the four-probe differential resistance, dV/dI, is plotted as a function of dc current bias I_{dc} at base temperature. Under application of an out-of-plane magnetic field B, the nonlinear behavior is clearly suppressed (Fig. 1E), as expected for superconductivity. These observations confirm a superconducting state forming in the monolayer atomic sheet, in contrast to its three-dimensional (3D) parent crystal, in which no superconductivity is found unless high pressure is applied (*24*, *25*). A small shoulder appears around 400 mK in the $R(T)$ curve (Fig. 1C). Although this may be an intrinsic feature of WTe_2, it could also result from the appearance of inhomogeneous superconducting islands as the temperature is reduced. We then characterize the superconducting transition by quantifying several important temperature scales. The onset of superconductivity, defined as the temperature at which R drops to 90% from its normal state, occurs at ~820 mK. Zero resistance is achieved at ~350 mK. Furthermore, we have also confirmed the 2D nature of the superconductivity by checking that the data fit the picture of a 2D Berezinskii-Kosterlitz-Thouless transition, with estimated critical temperature T_{BKT} ~ 470 mK (fig. S1). For simplicity in our discussion, we define the critical transition temperature T_c as the temperature at which R equals 50% of the normal state value. For the curve in Fig. 1C, T_c ~ 580 mK, as indicated. Similar behavior is observed in device 2, in which T_c is found to be as high as ~950 mK, although the resistance never drops to zero, owing to a known imperfection in this device [figs. S2 and S3, (*23*)]. In contrast to device 1, the $R(T)$ characteristic of device 2 is a good fit to the standard Aslamazov-Larkin and Maki-Thompson fluctuation conductivity terms (*26*, *27*) (fig. S1).

The observed superconductivity, and hence the monolayer's ground state, is easily gate-tunable. We reveal this aspect by plotting $R(T)$ for different V_{bg} (Fig. 2A), while V_{tg} is kept fixed at 5 V (all data in Fig. 2 is for device 1). One can clearly see a critical gate voltage V_c^{MIT} ~ −0.75 V at which a metal-to-insulator (MIT) transition occurs. At large gate voltages $V_{bg} > V_c^{MIT}$ (i.e., toward higher electron density), R decreases with decreasing T, and a zero-resistance state is observed at low enough temperature, indicating a superconducting phase. Slightly above V_c^{MIT}, there may exist an intrinsic metallic (nonsuperconducting) phase at zero temperature, but a more detailed study is necessary to confirm this, as the observed behavior near the transition may also be consistent with the formation of both superconducting and nonsuperconducting regions as a result of density inhomogeneities. By contrast, when $V_{bg} < V_c^{MIT}$ (i.e., lower electron density), R increases with decreasing T, pointing to an insulating ground state. This insulating behavior is consistent with the expectation for monolayer WTe_2 at low density: A topologically nontrivial insulating state exists at low temperatures (*19*–*21*), and edge-state conduction is known to be marginal for the measurement configuration of device 1 (*19*). Figure S2 shows a similar transition behavior for device 2. Given that the field effect is applied through a moderate dielectric constant material (κ_{BN} ~ 3.5), these observations demonstrate that the ground state of the monolayer can be easily tuned between the two extremes of electron transport in materials, that is, from the insulating to the superconducting state. For comparison, similar field-effect behavior in existing superconducting systems is achieved only by extreme charge-density doping using ionic liquids (*28*), using ultrahigh-κ dielectric materials such as $SrTiO_3$ (*29*, *30*), or ferroelectric polarization (*31*).

The gate tunability of the superconducting state can be further characterized by the extraction of the critical temperature and measurements of the critical current. In the upper panel of Fig. 2B, we plot the extracted $T_c(V_{bg})$, where one finds increasing T_c with increasing V_{bg}. Extrapolating to T_c = 0 K (red curve, see also fig. S4), we find a critical gate voltage V_{c1} ~ −0.65 V. The maximum observed T_c ~ 0.61 K appears at the highest applicable gate voltages for this device. Figure 2C shows dV/dI versus I_{dc} at $V_{bg} = V_{tg}$ = 5 V, where the sharp

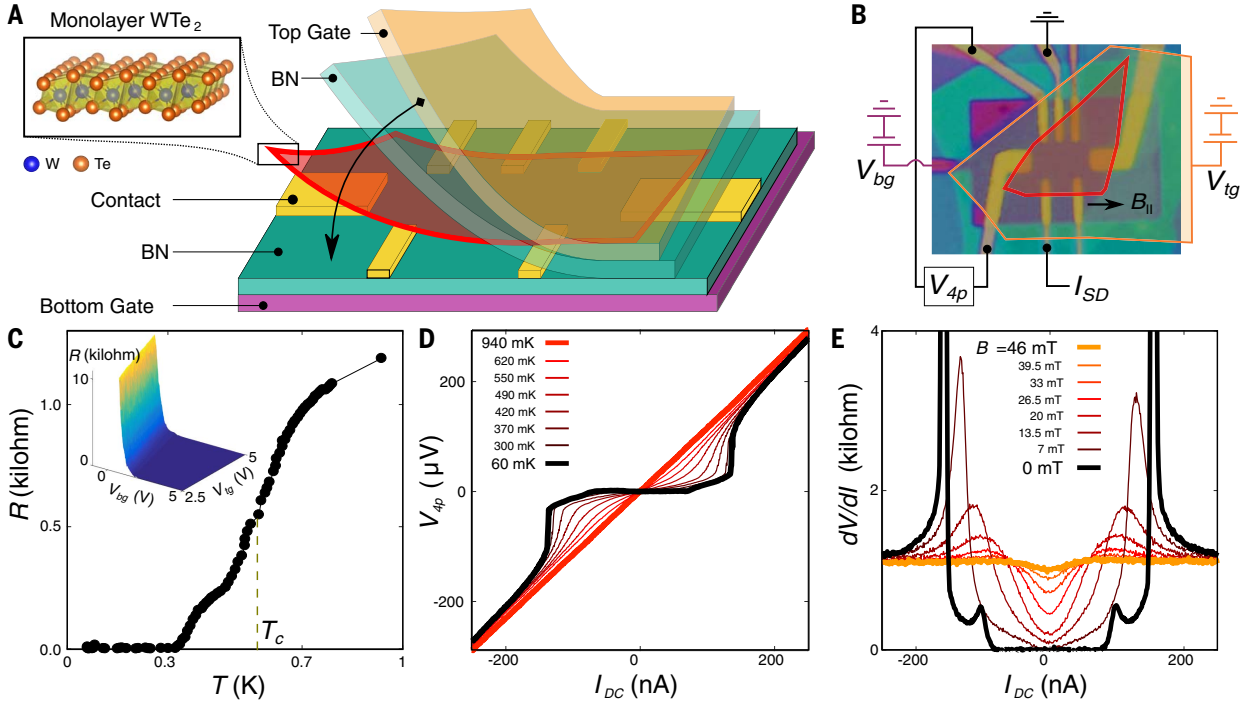

Fig. 1. Device schematic and superconductivity characteristics. (**A**) Cartoon illustration of the device structure and the crystal structure of monolayer WTe_2. (**B**) Optical microscopy image of device 1, with the monolayer WTe_2 (red) and graphite top gate (orange) highlighted. Circuit elements show the measurement configuration. V_{4p}, four-probe voltage; I_{SD}, source-to-drain current. (**C**) Temperature dependence of the resistance for V_{bg} = 4 V and V_{tg} = 5 V. The inset shows the resistance as a function of both gate voltages, at a base temperature of 60 mK. (**D**) *V-I* characteristics from base temperature (black) up to 940 mK (red). (**E**) Nonlinear *V-I* behavior, captured by differential resistance curves, at base temperature for different perpendicular magnetic fields.

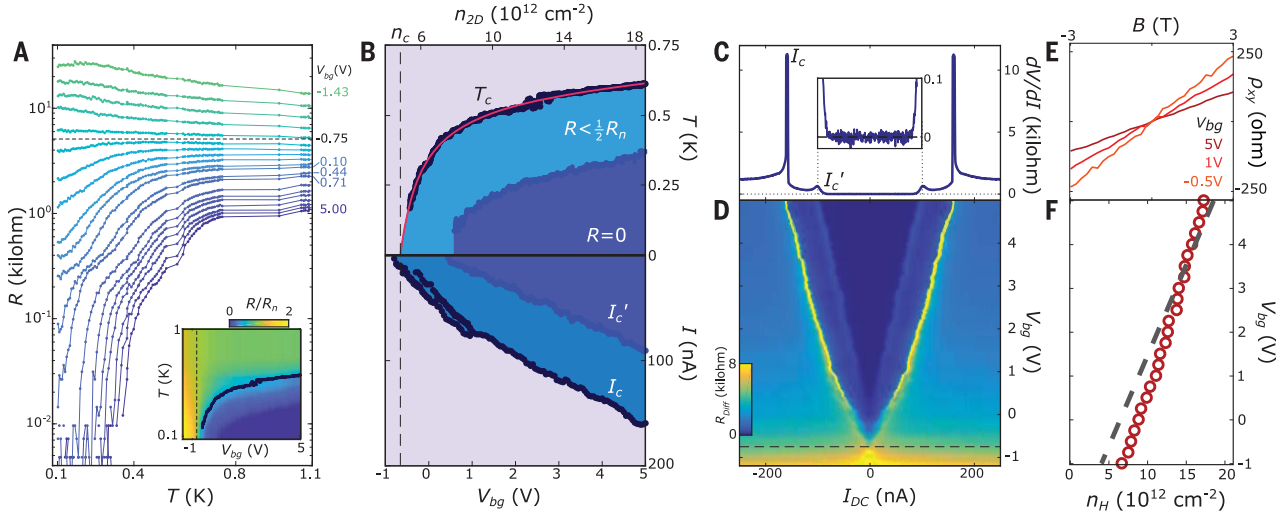

Fig. 2. Switching superconductivity on and off with an electrostatic gate. Shown are data from device 1. (**A**) *R*(*T*) characteristic for different gate voltages, showing the transition from a superconducting state to an insulating state, in evenly spaced increments between the labeled curves. The dashed line is a guide to the gate voltage, V_c^{MIT}, that separates the two regimes. The inset shows a color plot of the same data, normalized to the normal state resistance R_n, with T_c marked in black. (**B**) The upper panel shows the gate-dependent critical temperature T_c, summarized from (A). The zero-resistance region is shaded dark blue. The lower panel shows the gate-dependent critical current, I_c and I_c', summarized from (D). For V_{bg} < 1 V, I_c is found to bifurcate into two peaks, the values of which are determined by extrema of the second derivative of d*V*/d*I* (I_{dc}) data. The electron density (n_{2D}), corresponding to the bottom-gate voltage shown on the bottom axis, is estimated from the capacitance model and is shown on the top axis. (**C**) Differential resistance d*V*/d*I* versus current bias I_{dc} for V_{tg} = V_{bg} = 5V. The inset shows a zoom-in to the zero-resistance region. (**D**) Differential resistance (R_{diff}) d*V*/d*I* versus current bias I_{dc} and gate voltage V_{bg}. Close to V_{bg} ~ 1 V, the observed I_c trace bifurcates, as more clearly indicated in (B). The dashed line indicates the gate voltage at which the peaks in differential resistance merge at zero bias, indicating destruction of superconductivity. (**E**) Hall resistivity $\rho_{xy}(B)$ for three selected bottom-gate voltages taken at 2 K (V_{tg} = 5 V). See details in (*23*). (**F**) Extracted Hall density (n_H) as a function of the gate voltage (red circles) and the estimated density from the capacitance model (gray dashed line).

peak at the critical current $|I_{dc}| = I_c$ and the zero-resistance plateau for low currents demonstrate the expected behavior for superconductivity. The additional peak at $|I_{dc}| = I_c'$ in this dataset is consistent with the previously mentioned small shoulder in the $R(T)$ characteristic (Fig. 1C). The differential resistance is strongly modulated by gate voltage (Fig. 2D). The peaks at $\pm I_c$ monotonically shift toward zero bias with decreasing V_{bg} and eventually merge into a single peak at zero bias in the insulating region. This modulation of I_c is summarized in the lower panel of Fig. 2B, where we find that the critical gate voltage V_{c2}, at which I_c vanishes, falls in the range between −0.6 and −0.8 V.

Therefore, one finds that V_{c1}, V_{c2}, and V_c^{MIT} are very close to each other, which identifies the critical gate voltage as $V_{bg} = V_c \sim -0.7$ V (when $V_{tg} = 5$ V), above which superconductivity is exhibited. Using the capacitance model, we estimate the corresponding critical doping density as $n_c \sim 5 \times 10^{12}$ cm^{-2} (*23*). Hall effect measurements confirm a low absolute carrier density in the superconducting region that is consistent with the density estimates from the electrostatic capacitance model (Fig. 2, E and F, and details in fig. S5). The visible deviation appearing at lower doping in the plot may be related to inhomogeneous transport in the monolayer (e.g., the presence of conducting edge channels), which can introduce a minor factor to the measured Hall density. A similar critical density (~3×10^{12} cm^{-2}) is found in device 2 (*23*). These are among the lowest critical density values reported for 2D superconductors (*32*). Such low-density superconductivity in monolayer WTe_2 is the key to its extreme gate tunability. The maximum T_c obtained here (~0.6 K for device 1 and ~1 K for device 2, at carrier density $n_{2D} \sim 1.8 \times 10^{13}$ cm^{-2}) is relatively high, compared with other 2D superconductors with similar density (*30*, *32*).

The preliminary low-temperature electronic phase diagram of monolayer WTe_2 can now be summarized (Fig. 3A). The quantum spin Hall insulator (QSHI) phase resides near zero charge density, robust up to 100 K (*22*). With n-type doping above the critical density, n_c, the superconducting ground state develops at temperatures below T_c (superconductivity was not observed with p-type doping in the gate-accessible region). Above T_c, the system is metallic. The coexistence of QSHI and superconducting states in the same phase diagram establishes monolayer WTe_2 as a material for observing physics at the intersection of topological insulating states and superconductivity. In Fig. 3B, we show data from device 2, in which superconductivity and the quantized transport of the QSHI are observed in the same monolayer device. The helical edge transport in the QSHI phase in this device was characterized in detail in our previous report (*22*). Its superconducting behavior is characterized in fig. S3. These results therefore demonstrate the electrostatic field–effect switching of superconductivity on and off in a QSHI system. Moreover, in the same device, we also observed preliminary evidence that superconductivity can be introduced into the helical edge states by proximity effect via adjacent gate-induced superconducting regions (see details in fig. S6). In principle, such proximity-induced superconducting helical edge states can be used to construct devices hosting Majorana zero modes to study non-Abelian physics.

We further characterize the gate-tunable superconducting properties by examining the magnetic field dependence. As shown Fig. 4A, one finds an out-of-plane critical field at base temperature $B_{c2,\perp} \sim 30$ mT (for $V_{tg} = V_{bg} = 5$ V), at which half of the normal state resistance is recovered. The temperature and gate dependence of this critical field

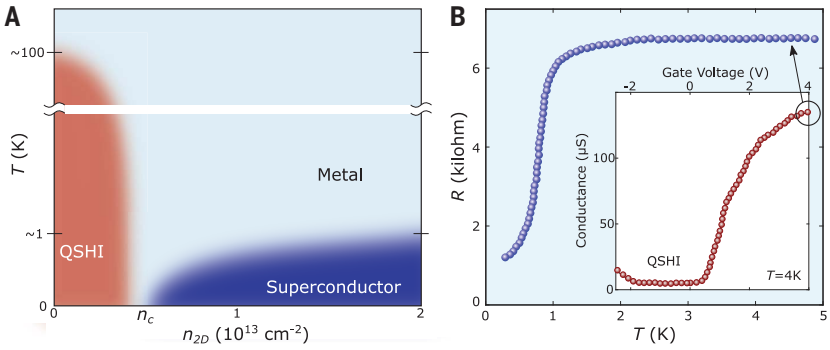

Fig. 3. Electronic phase diagram of monolayer WTe_2. (**A**) Schematic temperature-density phase diagram for the electronic ground state of monolayer WTe_2, reminiscent of the inset of Fig. 2A. (**B**) Resistance versus temperature for device 2, which shows a clear superconducting transition. The residual resistance at low temperature is caused by a known imperfection in this device, as described in (*23*). The inset shows the gate-dependent conductance of device 2, where the observed plateau corresponds to the QSHI phase. The arrow indicates the gate voltage at which the temperature dependence was recorded.

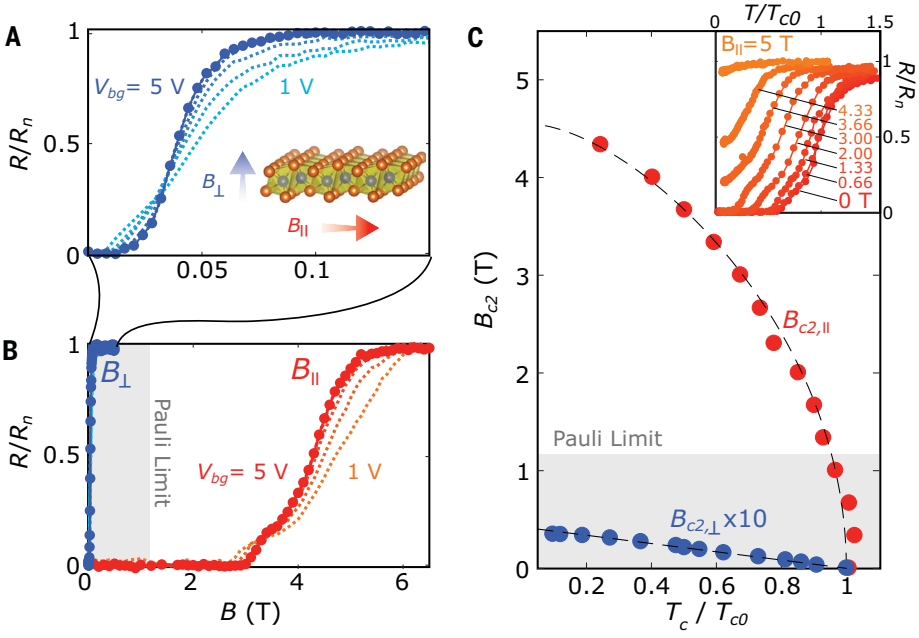

Fig. 4. Effect of magnetic field on the monolayer superconductivity. Shown are data from device 1. (**A**) Perpendicular magnetic field dependence of the resistance, $R(B_\perp)$, normalized to the normal state resistance R_n, at base temperature for different gate voltages: $V_{tg} = 5$ V and $V_{bg} = 5$, 4, 3, 2, or 1 V. The inset shows a schematic of the perpendicular and parallel field orientations. See Fig. 1B for the orientation of the parallel magnetic field in the plane of the device. (**B**) Comparison between effects of perpendicular and parallel fields. Orange represents the parallel magnetic field dependence of resistance, $R(B_{||})$, normalized to the normal state resistance R_n, for the same series of gate voltages as in (A). Blue represents the perpendicular magnetic field data of (A) plotted on the same scale for comparison. (**C**) B_{c2}-T_c phase diagram for both the parallel (orange) and perpendicular (blue) orientations. $V_{tg} = V_{bg} = 5$ V. Black dashed lines are fits to theoretical models (*23*). The inset shows the temperature dependence of resistance under different parallel magnetic fields.

is summarized in fig. S7, which indicates that the Ginzburg-Landau coherence length is close to 100 nm. This length is about an order of magnitude larger than the estimated transport mean free path (fig. S4), suggesting that the superconductivity is in the dirty limit. In contrast to the out-of-plane critical field, the in-plane critical field $B_{c2,\parallel}$ is substantially larger: About 4.3 T is required to recover half the normal state resistance (Fig. 4B). This field is about four times the conventional Pauli paramagnetic limit, which is given by $1.84T_c \sim 1.1$ T. We summarize the B_{c2}-T_c phase diagram for both the in-plane and out-of-plane cases in Fig. 4C. We note that the crystal symmetry and band structure of monolayer WTe_2 are very different from the transition metal dichalcogenides with hexagonal lattice structures, in which Ising-type superconductivity is responsible for exceeding the Pauli limit (*32*). Other possible mechanisms for exceeding the Pauli limit include reduced electron g-factor, spin-triplet pairing, or strong spin-orbit scattering (*33*, *34*). The superconductivity in the dirty limit is consistent with the spin-orbit scattering scenario (*33*, *34*), in which we extract a spin-orbit scattering time of ~244 fs [see fit in Fig. 4 and details in (*23*)]. However, we stress that our observations merit further study to understand the nature of the superconductivity and the exact mechanism for the large in-plane critical field in the WTe_2 monolayer.

We comment now on several interesting directions to explore. One is to look for an optimal doping, for example, to determine whether a superconducting dome exists in the phase diagram (*24*, *30*, *35*). Another is to investigate the effects of the material's strong anisotropy (*36*) and tunable noncentrosymmetry (*17*, *37*) on the superconductivity. A particularly interesting question is whether the observed superconductivity is topologically nontrivial. Although we currently do not have an answer, our results point to an exciting possibility of creating a 2D crystal–based topological superconductor using the proximity effect. Indeed, using local gates to achieve lateral modulation of superconducting and QSHI regions would enable the fabrication of tunable superconductor-QSHI-superconductor topological Josephson junctions (fig. S6) and the investigation of Majorana modes in a single material. In addition, van der Waals heterostructures that interface monolayer WTe_2 with materials such as the recently discovered 2D layered ferromagnets (*38*, *39*) can be developed for studying the interplay between superconductivity, magnetism, and topology.

REFERENCE AND NOTES

1. L. Fu, C. L. Kane, *Phys. Rev. Lett.* **100**, 096407 (2008).
2. M. Z. Hasan, C. L. Kane, *Rev. Mod. Phys.* **82**, 3045–3067 (2010).
3. X.-L. Qi, S.-C. Zhang, *Rev. Mod. Phys.* **83**, 1057–1110 (2011).
4. Y. S. Hor *et al.*, *Phys. Rev. Lett.* **104**, 057001 (2010).
5. L. A. Wray *et al.*, *Nat. Phys.* **6**, 855–859 (2010).
6. M. Einaga *et al.*, *J. Phys. Conf. Ser.* **215**, 012036 (2010).
7. J. L. Zhang *et al.*, *Proc. Natl. Acad. Sci. U.S.A.* **108**, 24–28 (2011).
8. P. P. Kong *et al.*, *J. Phys. Condens. Matter* **25**, 362204 (2013).
9. B. Sacépé *et al.*, *Nat. Commun.* **2**, 575 (2011).
10. S. Hart *et al.*, *Nat. Phys.* **10**, 638–643 (2014).
11. V. Mourik *et al.*, *Science* **336**, 1003–1007 (2012).
12. S. Nadj-Perge *et al.*, *Science* **346**, 602–607 (2014).
13. W. Chang *et al.*, *Nat. Nanotechnol.* **10**, 232–236 (2015).
14. H.-H. Sun *et al.*, *Phys. Rev. Lett.* **116**, 257003 (2016).
15. E. Bocquillon *et al.*, *Nat. Nanotechnol.* **12**, 137–143 (2017).
16. Q. L. He *et al.*, *Science* **357**, 294–299 (2017).
17. X. Qian, J. Liu, L. Fu, J. Li, *Science* **346**, 1344–1347 (2014).
18. F. Zheng *et al.*, *Adv. Mater.* **28**, 4845–4851 (2016).
19. Z. Fei *et al.*, *Nat. Phys.* **13**, 677–682 (2017).
20. S. Tang *et al.*, *Nat. Phys.* **13**, 683–687 (2017).
21. Z.-Y. Jia *et al.*, *Phys. Rev. B* **96**, 041108 (2017).
22. S. Wu *et al.*, *Science* **359**, 76–79 (2018).
23. See supplementary materials.
24. X.-C. Pan *et al.*, *Nat. Commun.* **6**, 7805 (2015).
25. D. Kang *et al.*, *Nat. Commun.* **6**, 7804 (2015).
26. V. V. Dorin, R. A. Klemm, A. A. Varlamov, A. I. Buzdin, D. V. Livanov, *Phys. Rev. B Condens. Matter* **48**, 12951–12965 (1993).
27. A. I. Larkin, A. A. Varlamov, *Theory of Fluctuations in Superconductors* (International Series of Monographs on Physics, Oxford Univ. Press, 2005).
28. Y. Saito, T. Nojima, Y. Iwasa, *Supercond. Sci. Technol.* **29**, 093001 (2016).
29. K. A. Parendo *et al.*, *Phys. Rev. Lett.* **94**, 197004 (2005).
30. A. D. Caviglia *et al.*, *Nature* **456**, 624–627 (2008).
31. C. H. Ahn *et al.*, *Science* **284**, 1152–1155 (1999).
32. Y. Saito, T. Nojima, Y. Iwasa, *Nat. Rev. Mater.* **2**, 16094 (2016).
33. R. A. Klemm, A. Luther, M. R. Beasley, *Phys. Rev. B* **12**, 877–891 (1975).
34. M. Tinkham, *Introduction to Superconductivity* (Dover, 2004).
35. J. T. Ye *et al.*, *Science* **338**, 1193–1196 (2012).
36. L. R. Thoutam *et al.*, *Phys. Rev. Lett.* **115**, 046602 (2015).
37. E. Bauer, M. Sigrist, Eds., *Non-Centrosymmetric Superconductors* (Lecture Notes in Physics Series, Springer, 2012), vol. 847.
38. B. Huang *et al.*, *Nature* **546**, 270–273 (2017).
39. C. Gong *et al.*, *Nature* **546**, 265–269 (2017).
40. S. Wu, Replication data for: Electrically tunable low-density superconductivity in a monolayer topological insulator. Harvard Dataverse (2018); https://doi.org/10.7910/DVN/UFGFY2.

ACKNOWLEDGMENTS

We thank L. Fu for helpful discussions and J. I.-J. Wang for assistance in operating the dilution refrigerator. **Funding:** This work was partly supported through AFOSR grant no. FA9550-16-1-0382 as well as the Gordon and Betty Moore Foundation's EPiQS Initiative through grant no. GBMF4541 to P.J.-H. Device nanofabrication was partly supported by the Center for Excitonics, an Energy Frontier Research Center funded by the DOE, Basic Energy Sciences Office, under award no. DE-SC0001088. This work made use of the Materials Research Science and Engineering Center's Shared Experimental Facilities supported by NSF under award no. DMR-0819762. Sample fabrication was performed partly at the Harvard Center for Nanoscale Science supported by the NSF under grant no. ECS-0335765. S.W. acknowledges the support of the MIT Pappalardo Fellowship in Physics. The WTe_2 crystal growth performed at Princeton University was supported by an NSF MRSEC grant, DMR-1420541. Growth of BN crystals was supported by the Elemental Strategy Initiative conducted by the MEXT, Japan, and JSPS KAKENHI grant nos. JP15K21722 and JP25106006. **Author contributions:** V.F. and S.W. fabricated the devices, performed electronic transport measurements, and analyzed the data. Y.C. and L.B. helped with measurements. Q.D.G. and R.J.C. grew the WTe_2 crystals. K.W. and T.T. grew the BN crystals. P.J.-H. supervised the project. V.F., S.W., and P.J.-H. co-wrote the manuscript with input from all co-authors. **Competing interests:** The authors declare no competing financial interests. **Data and materials availability:** Hexagonal boron nitride crystals were provided by K.W. and T.T. under a material transfer agreement with NIMS. All data needed to evaluate the conclusions in the paper are present in the paper or the supplementary materials and have been deposited at (*40*).

SUPPLEMENTARY MATERIALS

www.sciencemag.org/content/362/6417/926/suppl/DC1
Materials and Methods
Supplementary Text
Figs. S1 to S7
References (*41*–*47*)

12 November 2017; accepted 9 October 2018
Published online 25 October 2018
10.1126/science.aar4642

Electrically tunable low-density superconductivity in a monolayer topological insulator

Valla Fatemi, Sanfeng Wu, Yuan Cao, Landry Bretheau, Quinn D. Gibson, Kenji Watanabe, Takashi Taniguchi, Robert J. Cava and Pablo Jarillo-Herrero

Science **362** (6417), 926-929.
DOI: 10.1126/science.aar4642originally published online October 25, 2018

A monolayer of many talents

Superconductors with a topologically nontrivial band structure have been predicted to exhibit exotic properties. However, such materials are few and far between. Now, two groups show that the monolayer of the material tungsten ditelluride (WTe_2)—already known to be a two-dimensional topological insulator—can also go superconducting. Fatemi *et al.* and Sajadi *et al.* varied the carrier density in the monolayer by applying a gate voltage and observed a transition from a topological to a superconducting phase. The findings may lead to the fabrication of devices in which local gating enables topological and superconducting phases to exist in the same material.

Science, this issue p. 926, p. 922